Highly efficient and stable wide-bandgap perovskite solar cells via strain management

Xuegong Yu (yuxuegong@zju.edu.cn)
Zhejiang University
Pengjie Hang
Zhejiang University
Chenxia Kan
Zhejiang University
Biao Li
Zhejiang University
Yuxin Yao
Zhejiang University
Zechen Hu
Zhejiang University
Yiqiang Zhang
Zhengzhou University
Jiangsheng Xie
Sun Yat-sen University
Ying Wang
Zhejiang University
Deren Yang
Zhejiang University

Article

Keywords:

Posted Date: September 2nd, 2022

DOI: https://doi.org/10.21203/rs.3.rs-2014001/v1

Abstract

Wide-bandgap (WBG) perovskite solar cells (PSCs) with high performance and stability are in considerable demand in the photovoltaic market to boost tandem solar cell efficiencies. Perovskite bandgap broadening results in a high barrier for enhancing the efficiency of the PSCs and causes phase segregation in perovskite. In this study, we show that the residual strain is the key factor affecting the WBG perovskite device efficiency and stability. The DMSO addition not only helps lead halide to with opening the vertical layer spacing to form (CsI)0.08(PbI1.4Br0.6) and (CsI0.125Br0.875)0.08(PbI1.2Br0.8) intermediate phases, but also provide more nucleation sites to eliminate lattice mismatch with FAX (X = I, Br or Cl) or MAX, which dominates the strain effects on the WBG perovskite growth in a sequential deposition. By minimizing the strain, 1.67- and 1.77-eV nip devices with record efficiencies of 22.28% and 20.45%, respectively, can be achieved. The greatly enhanced suppression of phase segregation enables the device with retained 90% - 95% of initial efficiency over 4000 h of damp stability and 80% - 90% of initial efficiency over 700 h of maximum-power-point output stability under full-spectrum light without encapsulation. Besides, the 1.67-eV pin devices can achieve a competitive 22.3% efficiency while achieving considerable damp-heat, pre-ultraviolet (pre-UV) aging, and MPP tracking stability as per the tests conducted according to IEC 61215. The final efficiency for the perovskite/Si tandem is more than 28.3 %, which matches the top efficiencies reported to date.

Introduction

As the most promising next-generation photovoltaic technology, perovskite solar cells (PSCs) have achieved a record efficiency of 25.5%; these PSCs mainly comprise $FAPbI_3$ with a bandgap of ~1.5 eV[1-3]. Formamidinium (FA)-based PSCs with efficiencies over 23% almost employ perovskites with a bandgap below 1.6 eV due to that the low bromide (Br) and cesium (Cs) contents in the precursor solution make it easier to obtain high-quality and pure-phase perovskite[2-6]. With the efficiency approaching to the Schottky limit, a low-bandgap material such as Si, Pb-Sn perovskite and CIGS can be used to construct a tandem for further increasing the efficiency[7-9]. Efficient tandems require efficient PSCs with an optimal bandgap generally greater than 1.65 eV[10,11].

Because of the increased Br and Cs contents in perovskite, the bandgap increases while the efficiency and stability are limited mainly due to phase segregation[12,13]. The highest efficiency of the 1.65-eV WBG perovskite, which is widely applied in perovskite/Si 2-T tandems exceeds 20.5%, resulting in a final efficiency of over 29% in a tandem[7,10]. For all perovskite tandem systems, the optimal 1.77-eV-bandgap PSCs delivered the highest efficiency of ~16.5-17.5% due to the severe nonradiative recombination[8,14,15]. The performance of WBG PSCs is much worse than that of sub-1.6 eV PSCs; this hinders the development of perovskite-based tandems.

For the WBG perovskite, a thermodynamically stable Br-rich phase preferentially forms in the precursor solutions and films, resulting in multiple nonradiative recombination both in bulk perovskite and

interfaces with transport layers[16,17]. Halide migration can easily occur in defective perovskites with halide vacancies and grain boundary passages, resulting in phase segregation[18,19]. Hence, defect engineering is the commonly adopted strategy to mitigate phase segregation[20,21]. The partial substitution of the A site group by K^+, B site group by Sn^{2+} and X site group by Cl^- or SCN^- are known to improve the grain growth and eliminate defects to realize high-quality perovskites[22-25]. Yang et al. utilized tribromide to obtain customized defects in a 1.65 eV perovskite and achieved a high V_{OC} over 1.2 V; they finally prepared a perovskite/ Si tandem with 28.6% efficiency and good stability[26]. Surface passivation can indeed improve the performance of the WBG perovskite devices, a few of which can greatly enhance the device stability mostly based on the phase stability[27,28]. Each additional interface implies one more parasitic absorption, which is unfavorable for developing tandem solar cells.

Few efforts were made toward intrinsic carrier recombination management in WBG perovskite, demonstrating that such studies remain a challenge. Regardless, the strain in the perovskite is known to be a key factor that affects the induced defects, ion migration, component segregation, and lattice stabilization in perovskite, further dictating device's efficiency and stability[29-31]. Yang et al. confirmed that micro strain in $MAPb(I_{0.6}Br_{0.4})_3$ causes compositional inhomogeneity and phase segregation. By partially replacing Pb^{2+} with Sn^{2+}, the ion migration barrier can be increased and thus phase segregation can be mitigated[25]. Wang et al. added adenosine triphosphate (ATP) into 1.65-eV perovskite to modulate tensile strain and realized an illumination-stable nip perovskite/Si tandem solar cell[32]. However, the excellent tandem solar cells rely on efficient and stable perovskites with larger bandgaps (~ 1.7 eV) which suffer from severer performance loss and phase segregation.

Here, we developed a sequential method to fabricate WBG perovskite solar cells with state-of-the-art efficiencies of ~22.5% for 1.67-eV nip devices and ~20.3% for 1.77-eV nip devices, and ~22.3% for 1.67-eV pin devices. Strain analysis based on X-ray diffraction (XRD) patterns and Raman spectra were conducted for the film depositions. Careful control of layered-lead-halide-opening induced strain by DMSO in the precursor solution enables the transition from tensile strain to compressive strain in the perovskites. The strain-free WBG perovskite with exhibits the best phase stabilization under light soaking. The resultant nip devices have over 4000 h of storage stability and over 700 h of maximum-power-point (MPP) output stability under full-spectrum light without encapsulation. The resultant pin devices presented excellent performances in damp-heat, pre-UV aging and MPP tracking stability tests according to IEC 61215. By integrating these pin configurations on Si sub cells, an efficiency of over 28% can be achieved, demonstrating the valuable applications of the strain-free WBG PSCs.

Results

Strain characterization and analysis. In perovskite fabrication, methods are applied to first dissolve PbX_2 (X = I, Br, Cl) using DMF/DMSO and then to dissolve MAX or FAX using IPA. For WBG perovskite, it is necessary to add cesium addition to realize a specific bandgap and stabilize the phase[33]. Thus, CsX is introduced in the first deposition to form $(CsI)_{0.08}(PbI_{1.4}Br_{0.6})$ for 1.67-eV perovskite or

$(CsI_{0.125}Br_{0.875})_{0.08}(PbI_{1.2}Br_{0.8})$ for 1.77-eV perovskite films owing to its insolubility in IPA. The surface scanning electronic microscopy (SEM) morphologies of $(CsI)_{0.08}(PbI_{1.4}Br_{0.6})$ and $(CsI_{0.125}Br_{0.875})_{0.08}(PbI_{1.2}Br_{0.8})$ films with different DMSO contents are shown in Supplementary Fig. 1 and Fig. 2. The DMSO addition drastically enhances dendrite growth because of the supersaturation of the mesophase, which is shown in Supplementary Fig. 3 based on conventional XRD imaging results[16]. Compared to the XRD results of bare powders without DMSO treatment in Supplementary Fig. 4a, peaks newly generated at 8°-11°, which correspond to DMSO-related intermediate phases[34,35]. We carefully examined the black-circled PbI_2 peak position in Supplementary Fig. 4a; the details are shown in Supplementary Fig. 4b. The peak position shifts to smaller angles due to the DMSO addition, which indicates that the d spacing of PbI_2 increases probably with the strain effect. Furthermore, we conducted Fourier transform infrared (FTIR) spectroscopy measurements to verify the existence of DMSO, as shown in Supplementary Fig. 5. The overall peak position is basically inconsistent with the peak position in the DMSO IR spectrum. For the circled regions, which correspond to the S = O vibration and sp^3 CH bonding (DMSO fingerprint signals), DMSO clearly remains in the film. The d spacing determined through XRD with stress attachments is examined to determine the strain influence on $(CsI)_{0.08}(PbI_{1.4}Br_{0.6})$ and $(CsI_{0.125}Br_{0.875})_{0.08}(PbI_{1.2}Br_{0.8})$ films, as shown in Figs. 1a and 1b. According to the Bragg equation, the d-spacing increases as the azimuth angle (ψ) of the crystal plane increases. The linear fit of 2θ versus $\sin^2\psi$ illustrates the enhanced tensile strain for $(CsI)_{0.08}(PbI_{1.4}Br_{0.6})$ and $(CsI_{0.125}Br_{0.875})_{0.08}(PbI_{1.2}Br_{0.8})$ films, as shown in Figs. 1c and 1d[36,37]. The graphs of the tensile strain development with annealing temperature, as shown in Supplementary Figs. 6–11, illustrate that a higher temperature induces a larger tensile strain, which is corelated with the coefficient of thermal expansion (CTE) mismatch model[38,39]. The corresponding strain calculation formula is discussed in the Experimental Section. DMSO enters the atomic layers of lead halide and stretches the layers vertically or laterally to form a mesophase, which can be identified in the Raman spectra (Figs. 1e and 1f) [40–42]. The vertical arrangement is more conducive to the growth of vertically penetrating perovskite grains, which contributes to carrier transport. There are two signals that correspond to the laterally arranged lead halide at around 95 cm^{-1} and vertically arranged lead halide at ~ 110 cm^{-1}[40]. Introduction of DMSO reduced the contents of the laterally arranged $(CsI)_{0.08}(PbI_{1.4}Br_{0.6})$ and $(CsI_{0.125}Br_{0.875})_{0.08}(PbI_{1.2}Br_{0.8})$ intermediates, and the Raman peaks of both films shifted to a smaller wavenumber, indicating a tensile strain as proved by the XRD results[43,44].

With the further deposition of MAX/FAX dissolved in IPA, two WBG perovskite films with different bandgaps, as confirmed by the UV-Vis absorption spectra in Figs. 2a and 2b, were fabricated successfully. The absorption edges of these films are slightly different than those of films with the same perovskite composition due to the strain; the bandgaps of the two perovskite films are ~ 1.67 and 1.77 eV. The perovskite characteristics are distinguished using SEM, (Atomic force microscopy) AFM and XRD measurements. The tensile-strain induced precursor films with expanded lead hailed layers assist perovskite grain growth with DMSO content lower than 25% (Supplementary Fig. 12 and Fig. 13). However, the crystal grains become smaller when the DMSO content is 40%, possibly because of the

presence excessive perovskite nucleation centers. The largest average grain sizes are ~ 565 and 650 nm for 1.67-eV perovskite and 1.77-eV perovskites, respectively, with 25% DMSO. The AFM results in Supplementary Fig. 14 and Fig. 15 reconfirm the growth pattern. With DMSO increasement, more wrinkles appear on the perovskite surface, indicating the existence of compressive strain[45]. The XRD patterns in Supplementary Fig. 16 preliminarily indicate a more complete transformation from PbI_2 (red-circled in the SEM images in Supplementary Fig. 12 and Fig. 13) to the perovskite phase with increasing DMSO content. The compositional homogeneity on the perovskite surface or inside the perovskite is excluded from the SEM-EDS line-scan images (Supplementary Figs. 17–22). In the absence of MAI/MABr/FAI/FABr, the signal intensity of the halogens (Br or I) will be weakened, which is in agreement with the XRD results.

An eventual strain analysis was conducted on perovskite films by considering the XRD patterns shown in Figs. 2c and 2d. The fitting results from Figs. 2e and 2f prove that the residual tensile strain gradually transforms to compressive strain with an increase in DMSO with hardly any tensile strain after high-temperature annealing for both perovskites. Perovskite films with 25% DMSO have almost no residual stress or only have a slight stretching tendency. Nevertheless, high annealing temperatures still make perovskites tend to stretch, as shown from Supplementary Figs. 23–28; this stretching tendency promotes the transformation of the original compressive (tensile) strain to tensile (much more tensile) strain, accounting for the wrinkled perovskite surface with increased DMSO. Strain-free perovskite is less prone to generate lattice dislocation and defects (non-radiative recombination)[29,30,36]. The Raman measurements in Supplementary Fig. 29 further indicate that the strain is mainly applied on FA/MA-$[PbX_6]$ bonds, showing a tendency for compression versus DMSO increasement[46,47]. The charge carrier properties of SnO_2/perovskite films are delved using photoluminescence (PL) and time resolved photoluminescence (TRPL) tests as shown in Supplementary Fig. 30. As expected, perovskites with 25% DMSO had the strongest PL intensity, which indicates the least nonradiative recombination. A significant slower TRPL decay was recorded for strain-free perovskites with 25% DMSO in accordance with steady state PL tests[48–50]. Both tensile and compressive strains enable the carriers to form more nonradiative recombination centers in perovskites due to the stress effect.

Performance and stability of nip devices. Based on the above experimental results, we fabricated a whole solar cell with an ITO/SnO_2/Perovskite/Spiro-OMeTAD/Au structure. Their cross-sectional SEM images are shown in Supplementary Fig. 31 and Fig. 32. The performance and stability of the champion devices with different DMSO contents are illustrated in Fig. 3. Accordingly, strain-free, high-quality crystallinity, and low trap densities enabled us to realize the highest PCE of 22.28% with V_{OC} of 1.22 V, J_{SC} of 22.35 mA/cm^2 and *FF* of 80.35% for 1.67-eV PSCs, and the highest PCE of 20.45% with V_{OC} of 1.19 V, J_{SC} of 20.28 mA/cm^2 and recorded *FF* of 84.75% for 1.77-eV PSCs; these values are drastically than those of the strain-affected devices (Figs. 3a-3f). All photovoltaic performance parameters generally get improved, especially for V_{OC} and *FF* (Supplementary Fig. 33 and Fig. 34). The hysteresis also improved a lot with strain engineering. The J_{SC} and bandgap of perovskite were calibrated by external quantum efficiency

(EQE) in Supplementary Fig. 35, resulting in an integrated J_{SC} of 21.25 and 19.45 mA/cm^2. The detailed PV parameters of the state-of-the-art WBG perovskite solar cells are summarized in Supplementary Table 1, evidencing the breakthrough performance of our devices. The enhanced J_{SC} and *FF* in this study suggest that high-quality WBG perovskite with less defects can be obtained using the subsequent method as well as strain engineering.

The stability results are concluded in Figs. 3g and 3h. The unencapsulated devices for the target 1.67-eV WBG perovskite had almost no efficiency loss for the first 700 h in a N_2 glove box, and over 95% after the next 3500 h in the damp exposure with a relative humidity of 20–60%. Similarly, the target 1.77-eV WBG PSCs with more Br and Cs retained over 90% of their initial efficiency. However, the efficiency of 1.77-eV PSCs fluctuated more drastically, possibly because of the easier phase separation and recovery. To verify the tolerance under standard 1-sun illumination, the devices were placed traced by a solar simulator (Enli Tech.) without a filter in a nitrogen glovebox in Fig. 3h and Supplementary Fig. 36. The target 1.67-eV and 1.77-eV WBG PSCs retained over 90% and 80% of their initial efficiency after 700 h MPP tracking, respectively, competitively among the existing reported device stability values listed in Supplementary Table 2. Overall, regardless of dampness exposure and MPP tracking under light soaking, the strain-affected WBG PSCs degraded much more seriously, revealing the importance of strain control for WBG perovskite industrialization.

Effect of strain on phase stability. The photo-induced phase segregation of two WBG perovskites was carefully investigated and clarified via PL measurement in Fig. 4[51–53]. Here we utilized a Xenon lamp including UV region with an intensity of 2-sun to accelerate the segregation process. Light irradiated from the upper surface of perovskite to exclude the effect of tin oxide photocatalysis. For the 1.67-eV perovskite, obvious phase segregation occurred in the strain-affected perovskite, as shown in Figs. 4a and 4c, with prolonged light soaking. A second PL peak was observed at ~ 800 nm under tensile stress, whereas PL peak underwent a redshift under compressive stress, possibly resulting in poor MPP stability. A slight broadening of the PL peak of the strain-free perovskite in Fig. 4b suggests that no phase segregation occurred. The photo-stable perovskite film supports devices with enhanced MPP stability. For 1.77-eV perovskite from Figs. 4d-4f, the overall stability is poorer than that of the 1.67-eV perovskite due to more Br and Cs addition. Though phase segregation occurs in all films, it is less serious for the strain-free perovskite, which breeds a small peak at ~ 775 nm. The results also agree with the results of the stability tests in Figs. 3g, 3h and Supplementary Fig. 36.

Application expansion in pin and tandem solar cells. To further understand the universality of the process and concept, we fabricated pin solar cells with an ITO/NiO/perovskite/C60/BCP/Ag structure (Fig. 5a). Based on the similar thermal expansion coefficient of SnO_2 (1.17×10^{-5} K^{-1}) and NiO (1.2×10^{-5} K^{-1}), 1.67-eV perovskite with a default 25% DMSO content was not affected by strain[54,55]. The WBG solar cells with 25% DMSO exhibited a PCE of 22.31%, with V_{OC} of 1.21 V, J_{SC} of 22.40 mA/cm^2 and *FF* of 82.30%, thus outperforming the strained devices (Figs. 5b-5c). According to the IEC 61215 standard, we first tracked the damp-heat (80% RH, 80°C) tests, as shown in Fig. 5e, using sealed devices. The devices with

25% DMSO retained over 80% of their initial efficiency after 1000 h; however, they degraded rapidly with 10% or 40% DMSO. The devices exhibited less than 2% PCE loss after 80 h of UV exposure with the power of 60 kWh/cm^2, as shown in Fig. 5f. This is mainly due to the UV-insensitive of NiO layer. Finally, we performed the MPP tracking test for the devices (temperatures: 55℃ ± 5℃) under 1-sun illumination for 500 h without UV-cut. The devices with 25% DMSO can achieve over 82% of their initial efficiency, showing much better stability than the strained devices.

With the champion pin configuration adjusted to the Si heterojunction (SHJ) half cell (Fig. 5h), the following values were determined from the reverse *JV* curve in Fig. 5i: V_{OC} of 1.90 V, J_{SC} of 19.48 mA/cm^2, and *FF* of 76.42%. We achieved an overall efficiency of 28.35% with a minor hysteresis. With a MgF_2 antireflective layer, the integrated J_{SC} value of the perovskite sub cell was 19.43 mA/cm^2, which agrees well with the J_{SC} value of 19.28 mA/cm^2 for Si sub-cell (Fig. 5j). The integration directly in the tandem demonstrates a successful strain-free WBG perovskite application.

Discussions

We have summarized a simple preparation method for efficient and stable WBG PSCs via strain control. The photoinduced phase segregation in WBG perovskite is correlated with the intrinsic stability of strain-affected perovskite. Two PSCs with the bandgap of 1.67 and 1.77 eV commonly used in tandem solar cells were realized with record efficiencies of 22.28% and 20.45% for nip configuration to date. Furthermore, a state-of-the-art efficiency of 22.31% for 1.67-eV pin solar cells together with a competitive efficiency over 28% for the perovskite/Si tandem solar cells were obtained. The residual stress in perovskite can cause serious photoinduced phase segregation, reducing the stability of devices under continues light soaking. Both the target 1.67 eV and 1.77 eV nip WBG PSCs showed promising results, retaining over 90% and 80% of their initial PCEs after 700 h MPP tracking respectively. Further, the 1.67-eV pin WBG PSCs with restrained strain presented great damp-heat, pre-UV aging and MPP tracking stability tests with IEC 61215 standards. Strain effects on the efficiency and stability of WBG perovskites are critical, standing to be a key to facilitating the breakthrough of perovskite-based tandem solar cells.

Methods

Materials. Cesium iodide (CsI, 99.99%), Cesium bromide (CsBr, 99.99%), Lead (II) iodide (PbI_2, 99.99%), Lead (II) bromide ($PbBr_2$, 99.99%), C60 (>99.5% purity) and bathocuproine (BCP, >99.5% purity) were purchased from Xi'an Polymer Light Technology Corp. Spiro-OMeTAD (99.8%), methylammonium bromide (MABr, 99.9%), methylammonium chloride (MACl, 99.9%), Formamidinium iodide (FAI) and Formamidinium bromide (FABr) were purchased from Youxuan Tech. ITO was purchased from South China Xiangcheng Corp. Tin(IV) oxide, 15% in H_2O colloidal dispersion was purchased from Alfa Aesar. Nickle oxide (NiO_X) nanoparticle was purchased from Advanced Election Technology CO., Ltd. Other chemicals were purchased from Sigma-Aldrich except for special instructions.

Fabrication of nip WBG perovskite solar cells. For 1.67 eV perovskite solar cells, tin oxide nanocrystal aqueous solution diluted 5 times with deionized water was spin coated on UV-cleaned ITO at 3000 rpm for 30s, followed by 30 min annealing and 10-min UV treatment. Then, 1.5 M PbI_2/$PbBr_2$ (7:3, molar ratio) with 8.7% molar ratio of CsI in DMF/DMSO (9:1, 10%; 9:3, 25%; 9:6, 40%, volume ratio) was spin coated on SnO_2 at 1500 rpm for 30 s, followed by 1 min annealing at 70 ℃. After cooled down, the substrates was spin coated by a solution of FAI:MABr:MACl (77 mg:9.4 mg: 6.8 mg in 1 ml IPA) at 2000 rpm for 30s. The resultant films were thermal annealed at 150 ℃ for 15 min. A Spiro-OMeTAD layer was prepared by spin coating a solution of 72.25 mg Spiro-OMeTAD in 1 ml CB with 17.75 ul Li-salt solution (520 mg/ml in acetonitrile) and 28.75 ul tBp at 3000 rpm for 30 s. A 60-100 nm-thick gold was deposited using a thermal evaporator on the Spiro-OMeTAD film to form a completed device. For 1.77 eV perovskite film preparation, 1.5 M PbI_2/$PbBr_2$ (3:7, molar ratio) with 1.15%/7% molar ratio of CsI/CsBr in DMF/DMSO (9:1, 10%; 9:3, 25%; 9:6, 40%, volume ratio) was spin coated on SnO_2 at 1500 rpm for 30 s, followed by 2 min annealing at 50 ℃. After cooled down, the substrates was spin coated by a solution of FAI:FABr:MABr:MACl (53 mg:19.6 mg:7 mg: 6.8 mg in 1 ml IPA) at 2000 rpm for 30s. The resultant films were thermal annealed at 150 ℃ for 15 min. The preparation of other functional layers is the same as 1.67 eV PSCs fabrication.

Fabrication of pin WBG perovskite solar cells. The tin-doped indium oxide (ITO) glass was successively cleaned by sonication with deionized water, ethanol, acetone and isopropanol as agents followed by UV-ozone for 20 min. NiO_X nanoparticle (20 mg mL^{-1} in deionized water) was spin-coated on the ITO substrates at 4000 rpm for 30 s with post-annealed at 100 ℃ for 10 min in air. The preparation of the WBG perovskite films was the same as that in conventional nip structure. Then, 25 nm C60 and 5 nm BCP were thermally evaporated at a vacuum of < 3 × 10^{-4} Pa. The devices were completed with 100 nm Ag as electrodes.

Fabrication of perovskite/Si solar cells. Double-side-polished phosphorus-doped Czochralski silicon (Cz-Si) wafers were fabricated with a resistivity of 1-5 Ω/cm and a thickness of ~280 μm. The texturing process was conducted on one side of the wafer in alkaline solution to obtain the random pyramids. After RCA cleaning process, buffered oxide etching solution was used to remove the resulting oxide layer. Afterwards, the intrinsic, n- and p-type a-Si:H films were deposited by plasma-enhanced CVD with thicknesses of 8, 8 and 10 nm, respectively. A 40-nm-thick ITO layer was sputtered on the textured rear side with a 90/10 In_2O_3/SnO_2 target followed by a 200-nm-thick Ag layer. The ITO recombination layer (40 nm) was sputtered on the front polished side of the wafers. The Si bottom cells were next annealed at 200 ℃ for 10 min to recover the sputtering damage. For the fabrication of the perovskite top cells, the same NiO_X and WBG perovskite deposition as described above was implemented on the wafer. Subsequently, C60 (15 nm) was thermally evaporated at a rate of 0.1 Å s^{-1} onto the perovskite substrates. The thickness of the evaporated BCP was optimized up to 15 nm to compensate the loss of the IZO sputtering bombardment. 100 nm IZO (50 Ω/sq) was sputtered on the BCP layer with a 3-inch target

(In_2O_3/ZnO, 90%/10%) at a RF power of 50 W. Finally, Ag front electrodes (200 nm) and MgF_X antireflection films (100 nm) were formed by thermally evaporating at a rate of 0.8 Å s^{-1}.

Materials characterizations. Surface morphology and cross-sectional image of perovskite and the whole device were taken by a Field-Emission Scanning Electron Microscope (FESEM, S4800, Hitachi). Conventional XRD patterns of perovskite was tested by a D8 Discover (Bruker) with a Cu Kαradiation. While strain characterizations of the films were tested by X-ray diffractometer (Bruker D8, ADVANCE) with a stress attachment and a Raman spectrometer (Horiba Evolution). The bandgap of perovskite was determined using a UV–vis spectrometer (U-4100, Hitachi Limited). Here we conducted the PL measurements on samples with the structure of glass/patterned ITO/SnO_2/perovskite. The samples were excited from the glass side. The steady state PL measurements (FLS980) were performed a continuous Xenon light source (spot area 0.28 cm^2). The TRPL results were tested using a 405 nm excitation laser (repetition rate of 10 kHz, pulsed duration 60 ps, spot area 0.5 mm^2 and a photon flux of ~1 μJ/cm²). From these data, we extract the normalized PL intensity dividing the spectrum by maximum peak value (unit counts). The PL was collected with High-Gain Photomultiplier Tube (PMT) Detectors (Edinburgh). The step width was set up to 10 nm/s.

Device characterizations. Current density–voltage (J–V) curves were acquired under a simulated AM 1.5G illumination (94022A, Newport) using a Keithley 2400 in air, calibrated by a standard Si solar cell (PVM937, Newport) with KG5 filter. A 150 W xenon lamp (UXL-150MO, Ushio, Japan) was applied as a light source. All J-V characteristics were measured with a mask (0.056 cm^2). External quantum efficiency (EQE) spectra of devices were tested using a QE system (Model QEX10, PV Measurements, Inc.)

Device stability. For damp test, all the devices were stored under dark for the first 700 h in a nitrogen glove box and the next 3000 h in the ambient. Measure the efficiency every once in a while. For MPP test, each device with the considerable PCE (19-21% for 1.67 eV PSCs, 18-19 %for 1.77 eV PSCs) was output under the maximum power point in a nitrogen glove box using a Keithley 2400 Source Measure Unit with a solar simulator (Enli Technology Co., Ltd., SS-F5-3A) without temperature control (constant temperature maintained at 55±5℃) nor any filter. For damp-heat stability tests, all the devices were encapsulated and placed constant temperature and humidity test chamber (DB-TH, DANBLE). For pre-UV aging tests, the sealed devices were aged using a high-pressure mercury lamp (MUA-165, Cerma Precision, Japan).

Strain Calculation. For CTE mismatch model, the stress can be quantified as follows:

$$\sigma = \frac{E_T}{1 - v_T}(\alpha_S - \alpha_T)\Delta T \qquad (1)$$

where σ is the predicted stress due to the thermal expansion mismatch, E_T is Young's modulus of the target film, v_P is the Poisson's ratio of the target film, a_S and a_T are the respective thermal expansion of

the substrate and target films, and ΔT is the temperature gradient during cooling from the annealing temperature of the target film to room temperature. And the strain of the target film ε is obtained by dividing σ by E_T.

The measured strain can be obtained using classical $sin^2\psi$ equation where ψ is the crystal plane azimuth angle shown as follows:

$$\sigma = -\frac{E_T}{2(1-v_T)} ctg\theta_0 \frac{\pi}{180} \frac{\partial(2\theta_\varphi)}{\partial(sin^2\varphi)} = K\frac{\partial(2\theta_\varphi)}{\partial(sin^2\varphi)} \quad (2)$$

where θ_0 is the diffraction peak for stress free perovskite (hkl) crystal plane and $\theta\psi$ is the diffraction peak for the actual perovskite films, K is the simplified constant. For continuous, homogeneous isotropic materials, $2\theta_\psi \sim sin^2\psi$ is a strictly linear relationship with a slope, once the slop is determined, the related stain ε can be obtained.

Considering the d spacing, the strain ε can be defined as follows:

$$\varepsilon = \frac{d-d_0}{d_0} \quad (3)$$

where d is the measured d spacing, d_0 is the d spacing of strain-free films.

Data availability

The data that support the findings of this study are available from the corresponding authors upon reasonable request.

References

1. NREL Best Research Cell Efficiency Chart, https://www.nrel.gov/pv/assets/pdfs/best-research-cell-efficiencies-rev211214.pdf, Accessed February 2022.

2. Min, H. et al. Perovskite solar cells with atomically coherent interlayers on SnO_2 electrodes. *Nature* **598**, 444-450 (2021).

3. Kim, M. et al. Conformal quantum dot-SnO_2 layers as electron transporters for efficient perovskite solar cells. *Science* **375**, 302-306 (2022).

4. Yoo, J. J. et al. Efficient perovskite solar cells via improved carrier management *Nature* **590**, 587-593 (2021).

5. Jiang, Q. et al. Surface passivation of perovskite film for efficient solar cells. *Nat. Photonics* **13**, 460-466 (2019).

6. Hang, P. et al. Stabilizing fullerene for burn-in-free and stable perovskite solar cells under ultraviolet preconditioning and light soaking. *Adv. Mater.* **33**, 2006910 (2021).

7. Al-Ashouri, A. et al. Monolithic perovskite/silicon tandem solar cell with >29% efficiency by enhanced hole extraction. *Science* **370**, 1300-1309 (2020).

8. Lin, R. et al. All-perovskite tandem solar cells with improved grain surface passivation. *Nature* **603**, 73-78 (2022).

9. Han, Q. et al. High-performance perovskite/Cu(In,Ga)Se_2 monolithic tandem solar cells. *Science* **361**, 904-908 (2018).

10. Tan, H. et al. Dipolar cations confer defect tolerance in wide-bandgap metal halide perovskites. *Nat. Commun.* **9**, 3100 (2018).

11. Tong, J. et al. Wide-bandgap metal halide perovskites for tandem solar cells. *ACS Energy Lett.* **6**, 232-248 (2021).

12. Motti, S. G. et al. Phase segregation in mixed-halide perovskites affects charge-carrier dynamics while preserving mobility. *Nat. Commun.* **12**, 6955 (2021).

13. Knight, A. J. & Herz, L. M. Preventing phase segregation in mixed-halide perovskites: a perspective. *Energy Environ. Sci.* **13**, 2024 (2020).

14. Xiao, K. et al. All-perovskite tandem solar cells with 24.2% certified efficiency and area over 1 cm^2 using surface-anchoring zwitterionic antioxidant. *Nat. Energy* **5**, 870-880 (2020).

15. Lin, R. et al. Monolithic all-perovskite tandem solar cells with 24.8% efficiency exploiting comproportionation to suppress Sn(II) oxidation in precursor ink. *Nat. Energy* **4**, 864-873 (2019).

16. Huang, T. et al. Performance-limiting formation dynamics in mixed-halide perovskites. *Sci. Adv.* **7**, eabj1799 (2021).

17. Oliver, R. D. J. et al. Understanding and suppressing non-radiative losses in methylammonium-free wide-bandgap perovskite solar cells. *Energy Environ. Sci.* **15**, 714-726 (2022).

18. Yao, Y. et al. Phase-stable wide-bandgap perovskites for four-terminal perovskite/silicon tandem solar cells with over 30% efficiency. *Small* 2203319 (2022).

19. Futscher, M. H. & Deibel, C. Defect spectroscopy in halide perovskites is dominated by ionic rather than electronic defects. *ACS Energy Lett.* **7**, 140-144 (2021).

20. Barker, A. J. et al. Defect-assisted photoinduced halide segregation in mixed-halide perovskite thin films. *ACS Energy Lett.* **2**, 1416-1424 (2017).

21. Beal, R. E. et al. Structural origins of light-induced phase segregation in organic-inorganic halide perovskite photovoltaic materials. *Matter* **2**, 207-219 (2020).

22. Xu, J. et al. Triple-halide wide-band gap perovskites with suppressed phase segregation for efficient tandems. *Science* **367**, 1097-1104 (2020).

23. Abdi-Jalebi, M. et al. Maximizing and stabilizing luminescence from halide perovskites with potassium passivation. *Nature* **555**, 497-501 (2018).

24. Zhou, Y. et al. Stabilized wide bandgap perovskite solar cells by tin substitution. *Nano Lett.* **16**, 7739-7747 (2016).

26. Yang, G. et al. Defect engineering in wide-bandgap perovskites for efficient perovskite–silicon tandem solar cells. *Nat. Photon.* **16**, 588-594 (2022).

27. Duong, T. et al. Efficient and stable wide bandgap perovskite solar cells through surface passivation with long alkyl chain organic cations. *J. Mater. Chem. A* **9**, 18454-18465 (2021).

28. Wang, L. et al. Interface regulation enables hysteresis free wide-bandgap perovskite solar cells with low VOC deficit and high stability. *Nano Energy*, **90**, 106537 (2021).

29. Kim, G. et al. Impact of strain relaxation on performance of α-formamidinium lead iodide perovskite solar cells. *Science* **370**, 108-112 (2020).

30. Liu, D. et al. Strain analysis and engineering in halide perovskite photovoltaics. *Nat. Mater* **20**, 1337-1346 (2021).

31. Jones, T. W. et al. Lattice strain causes non-radiative losses in halide perovskites. *Energy Environ. Sci.* **12**, 596 (2019).

32. Wang, L. et al. Strain modulation for light-stable n-i-p perovskite/silicon tandem solar cells. *Adv. Mater.* **34**, 2201315 (2022).

33. Hu, Y. et al. Understanding the role of cesium and rubidium additives in perovskite solar cells: trap states, charge transport, and recombination. *Adv. Energy Mater.* **8**, 1703057 (2018).

34. Ren, Y. et al. New insight into solvent engineering technology from evolution of intermediates via one-step spin-coating approach. *Sci. China Mater.* **60**, 392-398 (2017).

35. Montecucco, R., Quadrivi, E., Po, R. & Grancini, G. All-inorganic cesium-based hybrid perovskites for efficient and stable solar cells and modules. *Adv. Energy Mater.* **11**, 2100672 (2021).

36. Zhu, C. et al. Strain engineering in perovskite solar cells and its impacts on carrier dynamics. *Nat. Commun.* **10**, 815 (2019).

37. Zhao, Y., Duan, J., Wang, Y., Yang, X. & Tang, Q. Precise stress control of inorganic perovskite films for carbon-based solar cells with an ultrahigh voltage of 1.622 V. *Nano Energy* **67**, 104286 (2020).

38. Xue, D.-J. et al. Regulating strain in perovskite thin films through charge-transport layers. *Nat. Commun.* **11**, 1514 (2020).

39. Rolston, N. et al. Engineering stress in perovskite solar cells to improve stability. *Adv. Energy Mater.* **8**, 1802139 (2018).

40. Baltog, I., Baibarac, M. and Lefrant, S. Quantum well effect in bulk PbI_2 crystals revealed by the anisotropy of photoluminescence and Raman spectra.*J. Phys.: Condens. Matter* **21**, 025507 (2009).

41. Sharma, R. et al. Lattice mode symmetry analysis of the orthorhombic phase of methylammonium lead iodide using polarized Raman. *Phys. Rev. Materials* **4**, 051601 (2020).

42. Buchanan, M., Bauhofer, W. and Martin, T. P. Impurity-induced Raman scattering in CsBr and CsI. *Phys. Rev. B* **10**, 4358-4363 (1974).

43. Wang, M., Ni, Z., Xiao, X., Zhou, Y. & Huang, J. Strain engineering in metal halide perovskite materials and devices: Influence on stability and optoelectronic properties. *Chem. Phys. Rev.* **2**, 031302 (2021).

44. Wu, J. et al. Nati. Sci. Rev., 2021, 8, nwab047. *Nati. Sci. Rev.* **8**, nwab047 (2021).

45. Bush, K. A. et al. Controlling thin-film stress and wrinkling during perovskite film formation. *ACS Energy Lett.* **3**, 1225-1232 (2018).

46. Ruan, S. et al. Raman spectroscopy of formamidinium-based lead halide perovskite single crystals. *J. Phys. Chem. C* **124**, 2265-2272 (2020).

47. Ghosh, S. et al. Vibrational study of lead bromide perovskite materials with variable cations based on Raman spectroscopy and density functional theory. *J. Raman Spectrosc.* **52**, 2338-2347 (2021).

48. Stolterfoht, M. et al. Visualization and suppression of interfacial recombination for high-efficiency large-area pin perovskite solar cells. *Nat. Energy* **3**, 847-854 (2018).

49. Kirchartz, T., Márquez, J. A., Stolterfoht, M. & Unold, T. Photoluminescence-based characterization of halide perovskites for photovoltaics. *Adv. Energy Mater.* **10**, 1904134 (2020).

50. Krückemeier, L., Krogmeier, B., Liu, Z., Rau, U. & Kirchartz, T. Understanding transient photoluminescence in halide perovskite layer stacks and solar cells. *Adv. Energy Mater.* 11, 2003489 (2021).

51. Zhao, H. et al. Phase segregation due to ion migration in all-inorganic mixed-halide perovskite nanocrystals. *Nat. Commun.* **10**, 1088 (2019).

52. Wang, Y. et al. Phase segregation in inorganic mixed-halide perovskites. *Photon. Res.* **8**, A56-A71 (2020).

53. Knight, A. J. et al. Halide segregation in mixed-halide perovskites: influence of A-site cations. *ACS Energy Lett.* **6**, 799-808 (2021).

54. Peercy, P. S. & Morosin, B. Pressure and temperature dependences of the Raman-active phonons in SnO_2. *Phys. Rev. B* **7**, 2779 (1973).

55. Nielsen, T. H. & Leipold, M. H. Thermal expansion of nickel oxide. *J. Am. Ceram. Soc.* **48**, 164 (1965).

Declarations

Acknowledgements

This project received funding from National Natural Science Foundation of China (No. 62025403, 61721005) and the Fundamental Research Funds for the Central Universities (226-2022-00200). We thank Science Compass for XRD and Raman measurements and analysis.

Author contributions

X. Y. and D. Y. supervised the whole project. P. H. conceived the idea and drafted the manuscript. P. H. and C. K. designed the experiments and fabricated the devices. B. L. and Y. Y. conducted most of strain analysis experiments. Z. H. contributed to the stability tests. Y. W. contributed to the SEM measurements. J. X. contributed to the analysis of tandem solar cells. X. Y., Y. Z. and D. Y. revised the manuscript. All authors contributed to the discussion of the paper.

Conflicts of interest

The authors declare no competing financial interests.

Figures

Figure 1

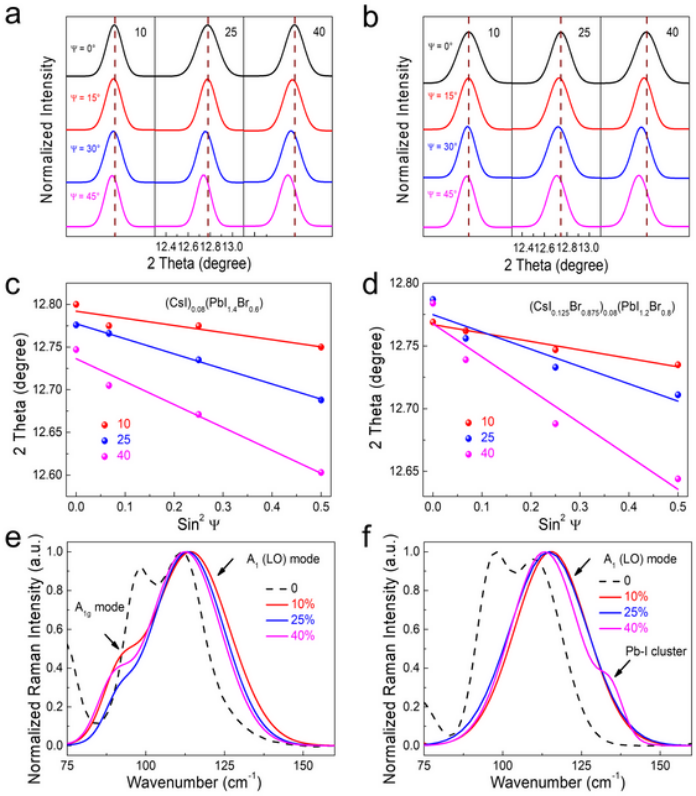

Figure 1

Characterization of the first spin-coated films. XRD patterns of **a** $(CsI)_{0.08}(PbI_{1.4}Br_{0.6})$ and **b** $(CsI_{0.125}Br_{0.875})_{0.08}(PbI_{1.2}Br_{0.8})$ films with different plane orientation angles. Strain distribution curves of **c** $(CsI)_{0.08}(PbI_{1.4}Br_{0.6})$ and **d** $(CsI_{0.125}Br_{0.875})_{0.08}(PbI_{1.2}Br_{0.8})$ films. Raman spectra of **e** $(CsI)_{0.08}(PbI_{1.4}Br_{0.6})$ and **f** $(CsI_{0.125}Br_{0.875})_{0.08}(PbI_{1.2}Br_{0.8})$ films using a 532 nm laser source.

Figure 2

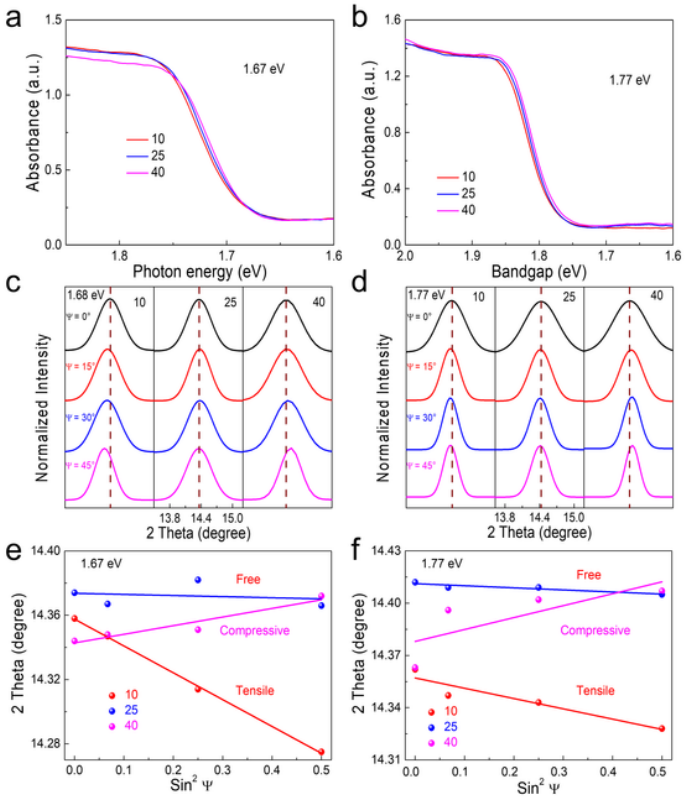

Figure 2

Characterization of the perovskite films. UV-vis spectra of 1.67-eV **a** and 1.77-eV **b** perovskites with different DMSO content (10%, 25%, 40%). XRD patterns of 1.67-eV **c** and 1.77-eV **d** WBG perovskite with different plane orientation angles. Strain distribution curves for 1.67-eV **e** and 1.77-eV **f** WBG perovskite.

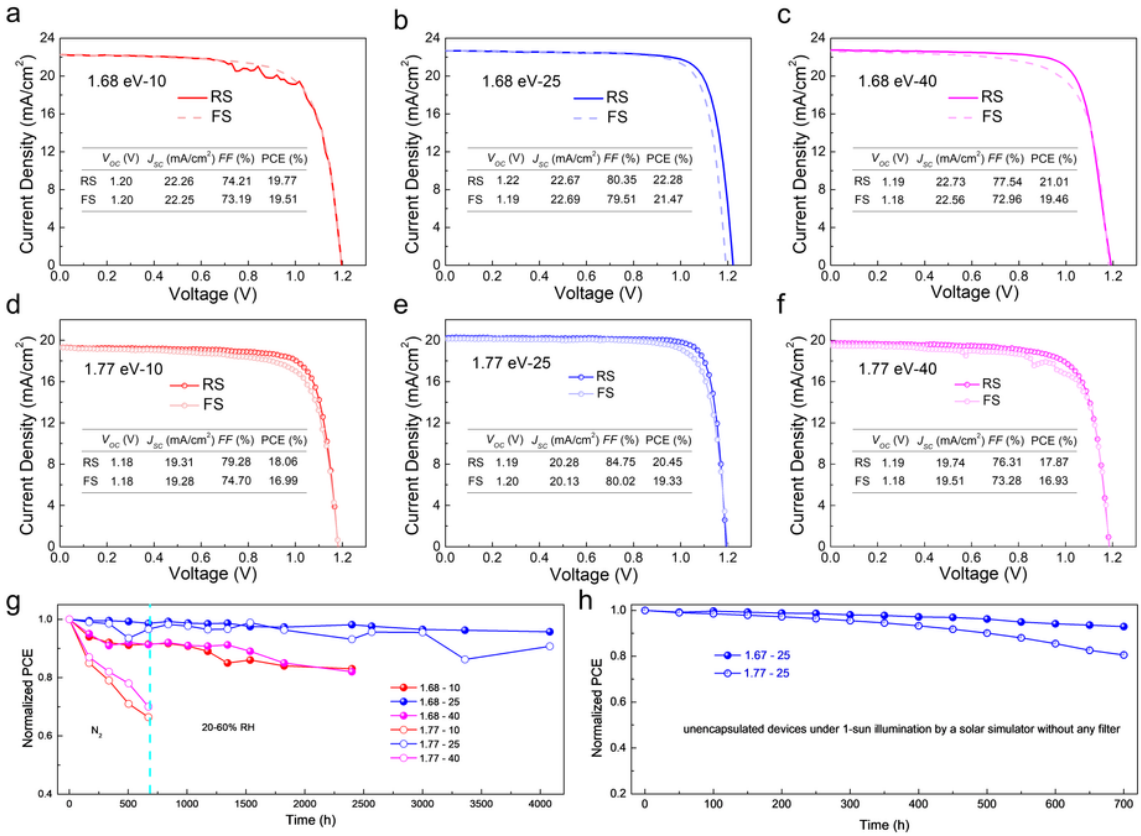

Figure 3

Figure 3

Performances and stabilities of nip structured devices. Current density – Voltage (*J-V*) curves of the champion device for 1.67-eV **a-c** and 1.77-eV **d-f** perovskite solar cells with different DMSO content. **g** The damp stability test of devices in the dark. **h** PCE tracking at the MPP of strain-free devices with two bandgaps.

Figure 4

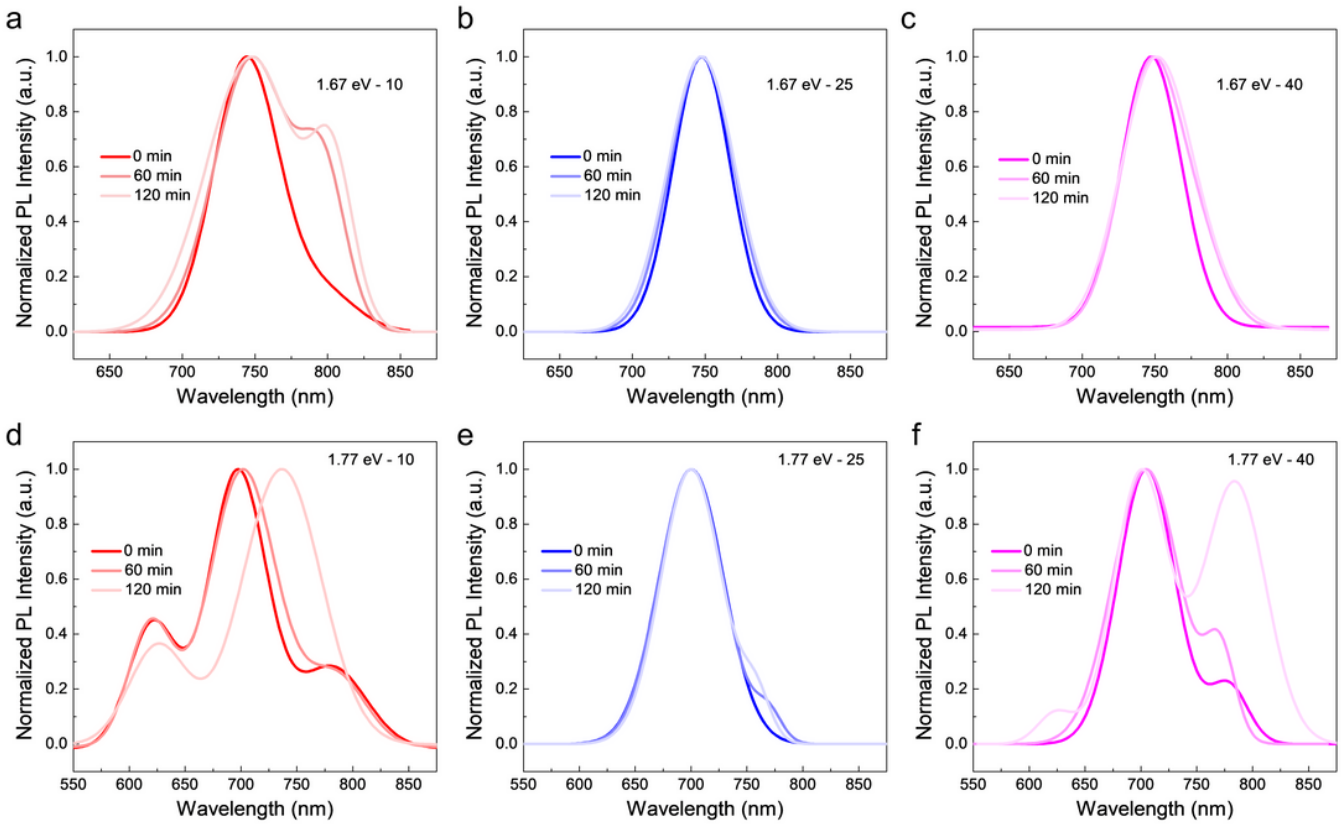

Figure 4

Phase segregation characterization. Photo-induced phase segregation investigation of 1.67-eV **a-c** and 1.77-eV **d-f** with different DMSO content (10%, 25%, 40%) by PL measurements.

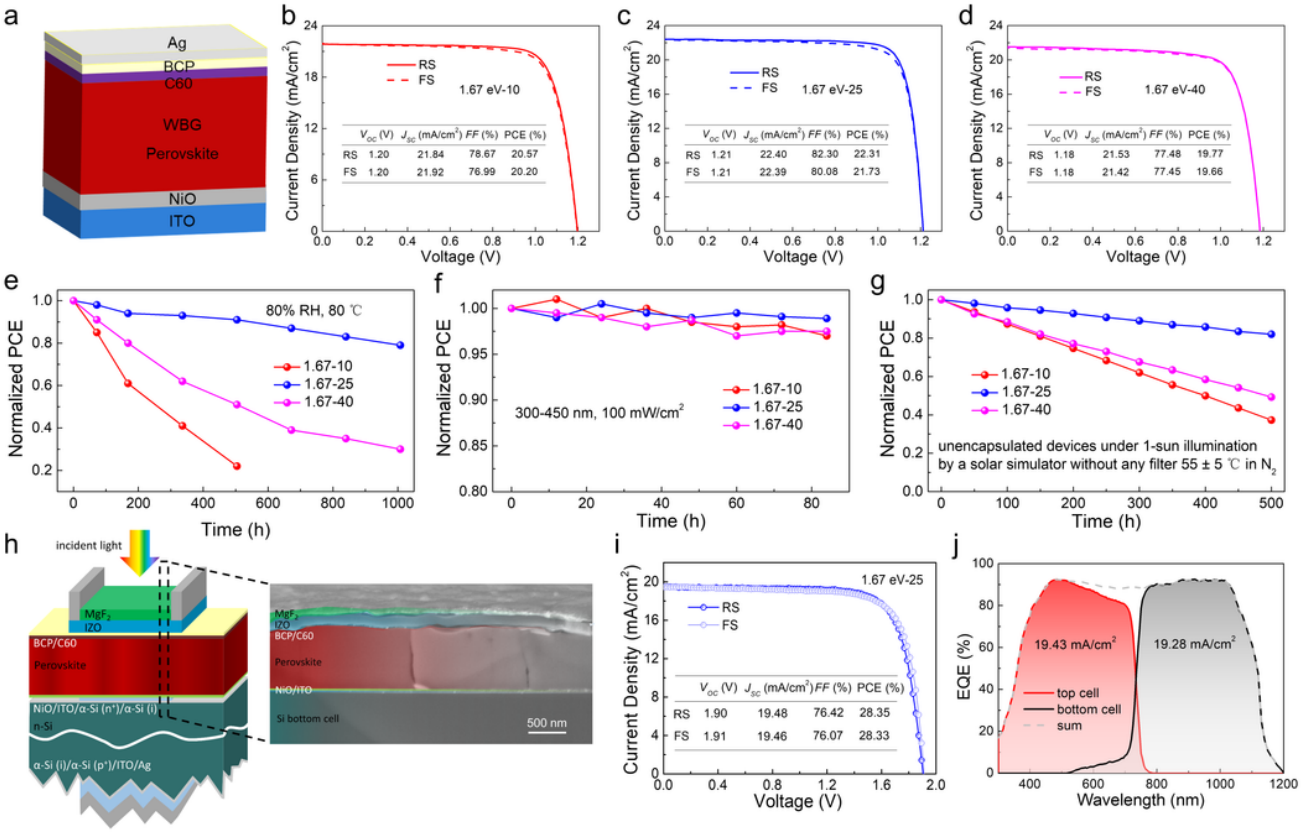

Figure 5

Performances and stabilities of pin structured devices. a Device configuration of pin single junction perovskite solar cells. Representative JV curves with corresponding PV parameters in Table for pin solar cells with 10% DMSO **b** 25% DMSO **c** and 40% DMSO **d**. Variation of normalized PCE of the sealed devices under damp-heat tests **e**, pre-UV aging tests **f** and MPP tracking stability tests **g**, **h** Device configuration with the cross-sectional SEM image of perovskite/Si tandem solar cells. **i** *JV* scan of the champion tandem solar cell. **j** EQE curves of the champion devices with bias lights.

Supplementary Files

This is a list of supplementary files associated with this preprint. Click to download.

- SI.docx